applied sciences

MDPI

Article

Dynamic Structural Response of a Corrugated Blast Wall Under Hydrogen Blast Loads

Hyunho Lee [1] and Jungkwan Seo [1,2,*]

[1] Department of Naval Architecture and Ocean Engineering, Pusan National University, Busan 46241, Republic of Korea; leehono@pusan.ac.kr
[2] The Korea Ship and Offshore Research Institute, Pusan National University, Busan 46241, Republic of Korea
* Correspondence: seojk@pusan.ac.kr

Abstract

A literature review was conducted to examine blast load characteristics of hydrogen, and the trend of hydrogen blast load and correlations between load characteristics were analyzed and compared with those of hydrocarbons. It was empirically confirmed that hydrogen explosions tend to produce higher peak overpressures and shorter durations compared with hydrocarbon explosions. In addition, blast load scenarios for hydrogen were selected considering the examined load characteristics and applied to numerical simulations. Dynamic structural responses of a corrugated blast wall were investigated through numerical simulations and analyzed from the perspective of displacement and strain energy. The results also indicated that blast walls designed for hydrocarbon explosions might not provide sufficient structural stiffness and strength to prevent excessive deflection and fracture under hydrogen blast loads. Lastly, a new type of diagram for structural response analysis was proposed, and deformation modes of corrugated blast walls were defined based on qualitative and quantitative structural responses.

Keywords: hydrogen blast load; dynamic structural response; deformation mode; corrugated blast wall; finite element method

check for updates

Academic Editor: Victor Giurgiutiu

Received: 27 June 2025
Revised: 18 July 2025
Accepted: 22 July 2025
Published: 24 July 2025

Citation: Lee, H.; Seo, J. Dynamic Structural Response of a Corrugated Blast Wall Under Hydrogen Blast Loads. *Appl. Sci.* **2025**, *15*, 8237. https://doi.org/10.3390/app15158237

Copyright: © 2025 by the authors. Licensee MDPI, Basel, Switzerland. This article is an open access article distributed under the terms and conditions of the Creative Commons Attribution (CC BY) license (https://creativecommons.org/licenses/by/4.0/).

1. Introduction

IMO [1] proposed a road map towards net-zero greenhouse gas (GHG) emissions by 2050 to contribute to global environmental protection and climate change response. Meanwhile, interest in eco-friendly energies that could replace existing hydrocarbon fuels is rapidly increasing in the shipbuilding and shipping industries, given the need to prevent greenhouse emissions. Liquefied natural gas (LNG), methanol, biofuel, ammonia, and hydrogen are all potential sources of eco-friendly shipping energy [2], and each has advantages and disadvantages in terms of greenness, cost-effectiveness, applicability, safety, and other criteria [3,4].

Among them, hydrogen is considered an ideal eco-friendly energy source because it can be produced through water electrolysis, has high combustion efficiency, and does not emit most of the harmful gases, such as carbon oxides, sulfur oxides, and fine dust, when used. However, due to its low boiling point, wide flammability limits, and low minimum ignition energy, hydrogen also possesses a high risk of explosion. In 2019, hydrogen explosion accidents occurred at a research facility in the Republic of Korea and a hydrogen fueling station in Norway [5,6]. These accidents clearly presented the high risk of hydrogen explosions and served as an opportunity to enhance safety regulations for hydrogen storage

facilities and promote research on hydrogen explosions. Nevertheless, due to the lack of relevant technology and research, further comprehensive studies need to be conducted to universalize and commercialize hydrogen energy.

When leaked or stored hydrogen explodes, strong pressure wave, and heat energy propagate to the surroundings. The pressure wave, in particular, can cause fatal failure and collapse of surrounding equipment and structures. Therefore, research analyzing dynamic structural response to blast loads is a useful reference when designing equipment and structures installed in a place with a high explosion risk. Mo et al. [7] predicted the dynamic structural response of a spherical tank exposed to a hydrogen-blended natural gas explosion through the Arbitrary Lagrangian–Eulerian (ALE) and TNT-equivalent methods and analyzed the effects of hydrogen blend ratio, pillar thickness, and explosive distance on the structural response. Wang et al. [8] observed the influence of volumetric blockage ratio on hydrogen explosion load and dynamic structural response by conducting a series of experiments and investigated the correlation of the blockage ratio with the structural response. Haghgoo et al. [9] conducted numerical simulations to investigate the influence of confined multi-point ignited H_2–O_2 mixtures on shock wave propagation and the dynamic response of thin plates, and the influence of the distance between the ignition location and the plate, as well as the combustion region, on the ultimate deformation of the plate was examined. Hao et al. [10] conducted 48 vented explosion experiments and analyzed the influence of vent position, the number of obstacles, ignition position, and hydrogen concentration on the dynamic structural response of a 40-foot container under hydrogen explosion loads. Du et al. [11] investigated the mode I crack propagation of a tube under internal hydrogen static and detonation loadings in terms of crack length and speed, energy storage, and other factors through numerical simulations. Russo et al. [12] applied a probabilistic risk assessment procedure to a high-pressure hydrogen pipeline to assess the harm to people and buildings exposed to pipeline explosions and proposed a safe distance from the pipeline network. In addition to the aforementioned studies, diverse research has been carried out to observe the dynamic response of various structures exposed to hydrogen explosions and obtained outstanding findings [13–22]. The literature review was conducted using Google Scholar with the keywords ‘structural response’ and ‘hydrogen explosion.’ The review focused on full papers and conference proceedings published after 2000 that were accessible through institutional resources. In addition, the AI-based tool Scite.ai was utilized to identify five studies that were most relevant and influential to this research. These studies were already included in the literature review, thereby confirming the comprehensiveness and relevance of the review.

However, most of the target structures investigated for dynamic structural response have been fundamental structures, such as storage tanks, simple plates or walls, and tunnels. In contrast, studies on hydrocarbon explosions have extensively investigated dynamic structural responses of both fundamental and practical structures, including steel frames, stiffened plates, reinforced concrete slabs, blast walls, nuclear power plants, and topside structures. Moreover, various studies have been conducted on diagrams, such as Pressure–Impulse (P–I) diagram and resistance curve, which can be utilized in the design of structures subjected to hydrocarbon blast loading. Unfortunately, such studies on hydrogen explosions are extremely rare, particularly in the shipbuilding and shipping industries.

In this study, a literature review was first conducted to collect and analyze experimental data on explosions, and blast load characteristics of hydrogen were examined. The trend of hydrogen blast loads and the correlations between load characteristics were analyzed and compared with those of hydrocarbons. Moreover, the dynamic structural response of a target structure was investigated under various hydrogen blast load scenarios that reflect the examined load characteristics, using a numerical model created in LS-DYNA [23]. A

corrugated blast wall, commonly employed in offshore structures to prevent the propagation of blast loads, was selected as the target structure. Lastly, a new type of diagram and deformation modes for analyzing the dynamic structural response of corrugated blast walls were proposed. The objective of this study is to investigate the dynamic structural response of a corrugated blast wall, originally designed for hydrocarbon explosions, when subjected to hydrogen blast loads. The findings are expected to contribute to the advancement of safety standards and structural design practices in the shipbuilding and offshore industries.

2. Blast Load Characteristics of Hydrogen and Hydrocarbons: A Review

A literature review was conducted on studies published after 2000 that had carried out explosion experiments. No restrictions were imposed on experimental conditions, such as geometric conditions or types and concentrations of combustible materials, to ensure the generality of the literature review. As a result, experimental data from 33 papers were analyzed [10,24–55]. However, data for which a duration was not observed were excluded from the review, and negative phases of blast load were also not included. The information on each paper is summarized in Tables 1 and 2. These tables are categorized by the type of combustible material used in the explosion experiments. The 'No.' shown in the first column of the tables is used to identify the source of experimental data in subsequent figures.

Table 1. Summary of experimental studies on hydrocarbon explosions.

No.	Title	Geometric Condition	Combustible/ Flammable Material Type	Concentration or Amount	Authors
HC1	Venting of gas explosion through relief ducts: interaction between internal and external explosions	Cylindrical vessel and duct	Propane	Stoichiometric and rich-fuel conditions	Ferrara et al. (2008) [25]
HC2	Vented explosion overpressures from combustion of hydrogen and hydrocarbon mixtures	Vented chamber	Methane and propane	Methane: 9.5%, propane: 4.0%	Bauwens et al. (2011) [26]
HC3	Explosion characteristics of argon/nitrogen-diluted natural gas–air mixtures	Spherical vessel	Natural gas	5.5–15.0 vol. %	Zhang et al. (2014) [27]
HC4	Experimental study on explosion characteristics of ethanol–gasoline–air mixture and its mitigation using heptafluoropropane	Vented rectangular vessel	E10 (mixture of ethanol and unleaded gasoline)	0.8–1.8 mL	Li et al. (2019) [28]
HC5	Experimental study of hydrogen explosion in repeated pipe congestion—Part 2: Effects of increase in hydrogen concentration in hydrogen–methane–air mixture	Congestion rig	Methane	1.16 kg	Shirvill et al. (2019) [29]

Table 1. *Cont.*

No.	Title	Geometric Condition	Combustible/ Flammable Material Type	Concentration or Amount	Authors
HC6	Experimental study on the deflagration characteristics of methane–ethane mixtures in a closed duct	Square duct	Methane and ethane	Notated in the paper	Luo et al. (2020) [30]
HC7	Effects of gas concentration and obstacle location on overpressure and flame propagation characteristics of hydrocarbon fuel–air explosion in a semi-confined pipe	Semi-confined pipe	Gasoline vapor	1.3–2.1%	Li et al. (2021) [31]
HC8	Gas explosions of methane–air mixtures in a large-scale tube	Squared tube	Methane	9.5 vol. %	Li et al. (2021) [32]

Table 2. Summary of experimental studies on hydrogen explosions.

No.	Title	Geometric Condition	Combustible/ Flammable Material Type	Concentration or Amount	Authors
H1	A field explosion test of hydrogen–air mixtures	Tent	Hydrogen	Notated in the paper	Wakabayashi et al. (2005) [33]
H2	Large-scale experiments: deflagration and deflagration-to-detonation transition within a partial confinement similar to a lane	Lane		37–41 vol. %	Schneider (2005) [34]
H3	Experiments on hydrogen deflagration	Prismatic tent		30%	Sato et al. (2006) [24]
H4	Hydrogen explosion study in a confined tube: FLACS CFD simulations and experiments	Square-section steel tube		20%	Middha et al. (2007) [35]
H5	Large-scale hydrogen deflagrations and detonations	Diverse		Notated in the paper	Groethe et al. (2007) [36]
H6	An inter-comparison exercise on CFD model capabilities to predict a hydrogen explosion in a simulated vehicle refueling environment	Refueling station congestion		Equivalence ratio of 1.1	Makarov et al. (2009) [37]
H7	Vented explosion overpressures from combustion of hydrogen and hydrocarbon mixtures	Explosion test chamber with a square vent		18%	Bauwens et al. (2011) [26]
H8	Effect of hydrogen concentration on vented explosion overpressures from lean hydrogen–air deflagrations	Test chamber with square vent		12–19 vol. %	Bauwens et al. (2012) [38]

Table 2. *Cont.*

No.	Title	Geometric Condition	Combustible/ Flammable Material Type	Concentration or Amount	Authors
H9	Experimental study on premixed hydrogen/air and hydrogen–methane–air mixtures explosion in 90-degree bend pipeline	90-degree pipeline	Hydrogen	Equivalence ratios of 0.13–0.30	Emami et al. (2013) [39]
H10	Fundamental study on accidental explosion behavior of hydrogen–air mixtures in an open space	Open space		Equivalence ratios of 0.7–4.0	Kim et al. (2013) [40]
H11	Effects of hydrogen on combustion characteristics of methane in air	Closed spherical vessel		20.13–38.65%	Ma et al. (2014) [41]
H12	A study on the characteristics of the deflagration of hydrogen–air mixture under the effect of an aluminum alloy mesh	Test tube		30%	Pang et al. (2015) [42]
H13	Effect of burst pressure on vented hydrogen–air explosion in a cylindrical vessel	Cylindrical vessel with a neck		Equivalence ratio of 2.0	Guo et al. (2015) [43]
H14	Medium-scale experiments on vented hydrogen deflagration	Test chamber with square vent		7–50%	Kuznetsov et al. (2015) [44]
H15	Effect of ignition location on external explosion in hydrogen–air explosion venting	Cylindrical vessel		49 vol. %	Cao et al. (2017) [45]
H16	Explosion venting of rich hydrogen–air mixtures in a small cylindrical vessel with two symmetrical vents	Vented vessel		Equivalence ratio of 2.0	Guo et al. (2017) [46]
H17	Experimental study of hydrogen explosion in repeated pipe congestion—Part 2: effects of increase in hydrogen concentration in hydrogen–methane–air mixture	Congestion rig		Pure hydrogen	Shirvill et al. (2019) [29]
H18	Experimental and theoretical evaluation of hydrogen cloud explosion with built-in obstacles	Cubic frame with built-in obstacles		29.57 vol. %	Li et al. (2020) [47]
H19	Experimental study on the effects of ignition location and vent burst pressure on vented hydrogen–air deflagrations in a cubic vessel	Cubic vessel		Stoichiometric condition	Rui et al. (2020) [48]
H20	Evaluation of unrestricted hydrogen and hydrogen–methane explosion venting through duct	Spherical explosion chamber		Equivalence ratios of 0.6–3.5	Li et al. (2021) [49]
H21	Experimental investigation on the dynamic responses of vented hydrogen explosion in a 40-foot container	40-foot carbon steel container with vent		12–24%	Hao et al. (2021) [10]
H22	Effect of hydrogen concentration on the vented explosion of hydrogen–air mixtures in a 5 m long duct	Rectangular duct		10–40%	Zhang et al. (2022) [50]

Table 2. *Cont.*

No.	Title	Geometric Condition	Combustible/ Flammable Material Type	Concentration or Amount	Authors
H23	Experimental study on external explosion for vented hydrogen deflagration in a rectangular tube with different vent coefficients	Rectangular tube	Hydrogen	14–18 vol. %	Wang et al. (2022) [51]
H24	Investigation on unconfined hydrogen cloud explosion with external turbulence	Unconfined fan-stirred explosion setup		Equivalence ratios of 0.8–3.0	Jiang et al. (2022) [52]
H25	The effect of gas jets on the explosion dynamics of hydrogen–air mixtures	Spherical explosion container		Notated in the paper	Chang et al. (2022) [53]
H26	Visualization of the external flow field during a vented explosion for hydrogen–air mixtures: effects of hydrogen concentrations and vent areas	Cylindrical tube		30 vol. %	Song et al. (2022) [54]
H27	Reenacting the hydrogen tank explosion of a fuel-cell electric vehicle: an experimental study	Hydrogen car at outdoor site		Notated in the paper	Park and Kim (2023) [55]

For clarity, it is explicitly stated that Figures 1–4 are based on data extracted from previously published studies. Figure 1 shows several blast loads of hydrocarbons and hydrogen as time series data. Since presenting all time series data would make analysis challenging due to the large amount of data, only blast loads with maximum and minimum peak overpressure (p_{peak}), maximum and minimum rising time (t_r), and maximum and minimum duration (t_d) are shown. The reference number for each blast load is marked in square brackets, and blast loads corresponding to very short time and low overpressure ranges are enlarged and presented in the red dotted boxes. It can be observed that the overpressure of hydrogen explosions tends to be greater than that of hydrocarbons, and the rising time and duration of hydrocarbon explosions tend to be longer than those of hydrogen. This is because hydrogen has a higher combustion rate and flame propagation speed than hydrocarbons during explosions [56,57]. Moreover, in the case of hydrogen, a great difference in scale between blast loads was observed depending on explosion conditions. This shows uncertainty and a high risk of hydrogen explosions because an unpredictable blast load might be caused by a slight change in conditions.

Figures 2 and 3 present correlations between peak overpressure, duration, and rising time, which are representative blast load characteristics obtained from all time series blast loads. Peak overpressure, duration, and rising time are defined as the maximum overpressure, the time from the occurrence of overpressure to the point when the overpressure becomes zero, and the time from the occurrence of overpressure to the peak overpressure, respectively. For gas explosions, the duration is often found to be inversely proportional to the peak overpressure. Furthermore, an equation linking the peak overpressure and duration has been derived [58].

Figure 2a presents the correlation between peak overpressure and duration for hydrocarbon blast loads, divided into three regions. To determine boundaries between the regions, the data in Figure 2a were first grouped based on data trend and confinement level of explosion test environments. Regression analysis was then conducted for each group of data to derive trend lines in the form of inverse proportional functions. Median lines between these trend lines were used as the boundaries to divide the regions. In Region I, high

peak overpressures and very long durations were observed. These blast load characteristics were because experiments in Region I were conducted in long tunnel-type closed ducts, and any unburned gas that did not escape into the atmosphere sufficiently combusted. Region II is characterized by high peak overpressures and relatively long durations. The experiments in Region II were conducted in quasi-confined explosion chambers, and there was more unburned gas than in the experiments in closed ducts because the exhaust was carried out through narrow pipes. Moreover, durations were shorter than in Region I because chamber and measurement conditions were symmetric, unlike the experiments in Region I. Lastly, Region III exhibits load characteristics that are either consistent with the equation proposed by Høiset et al. [58] or with much weaker overpressures and shorter durations. Load characteristics consistent with the equation tended to be observed when vent openings existed in explosion chambers. This supports the recommendation that the equation should be used for predicting blast load characteristics in partially confined spaces. In contrast, for explosion experiments conducted under extremely low confinement conditions or for small-scale phenomena, blast loads were characterized by peak overpressures and durations less than 0.1 MPa and 0.1 s, respectively.

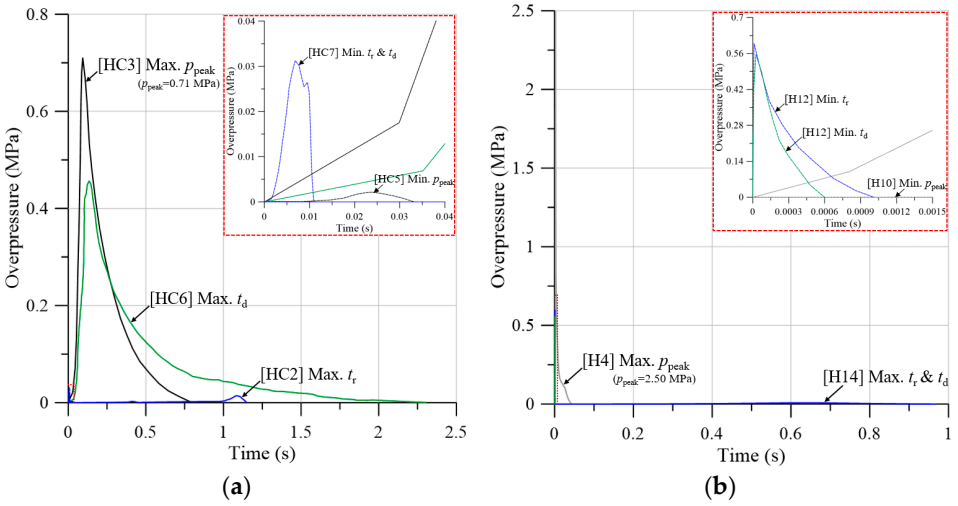


Figure 1. Time-overpressure curves based on experimental data for (**a**) hydrocarbon and (**b**) hydrogen explosions.

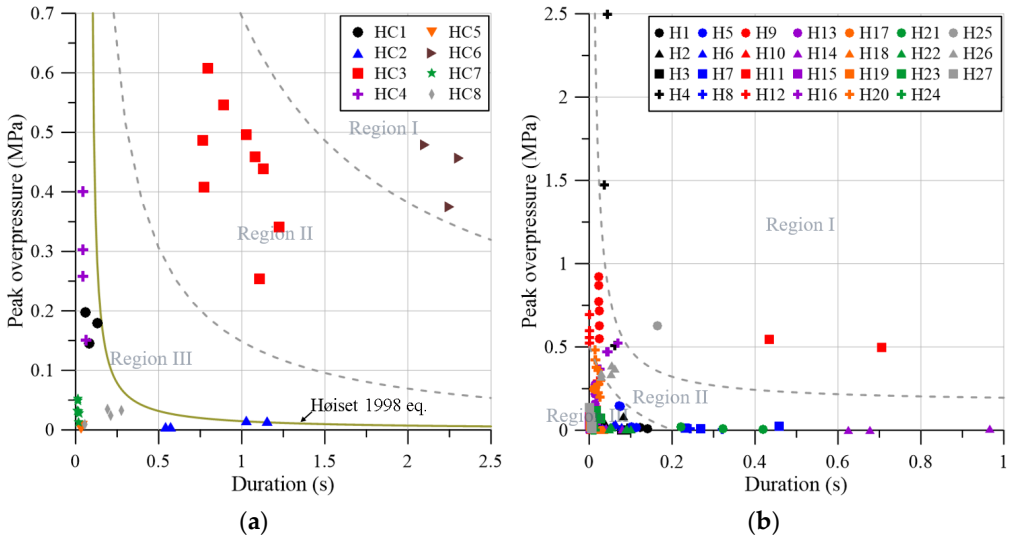


Figure 2. Experimental correlations between peak overpressure and positive phase duration for (**a**) hydrocarbon and (**b**) hydrogen explosions [58].

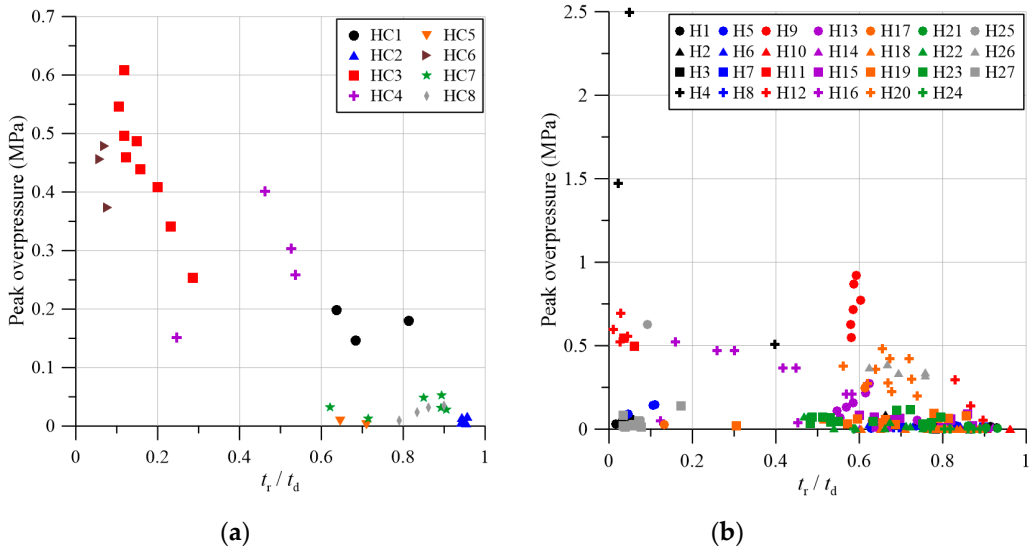


Figure 3. Experimental correlations between peak overpressure and rising time-to-duration ratio for (**a**) hydrocarbon and (**b**) hydrogen explosions.

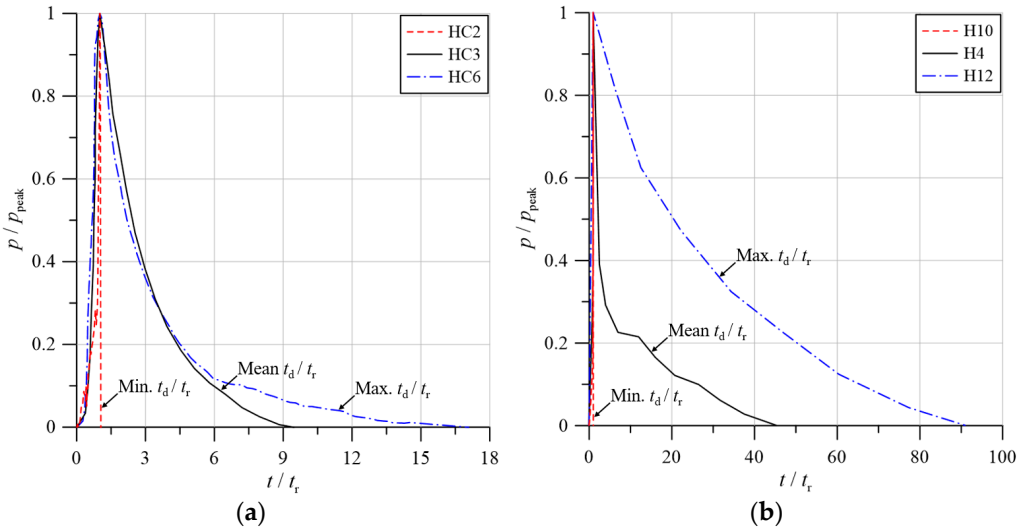


Figure 4. Nondimensionalized time-nondimensionalized overpressure curves based on experimental data for (**a**) hydrocarbon and (**b**) hydrogen explosions.

Figure 2b presents the correlation between peak overpressure and duration for hydrogen blast loads and is also divided into three regions by applying the same methodology as for hydrocarbons. Blast load characteristics of hydrogen explosion experiments conducted in quasi-confined chambers or relatively large-scale tunnels are mostly located in Region I, while those of experiments conducted in pipes or chambers with vent openings are predominantly located in Region II. Lastly, load characteristics of experiments conducted under low confinement conditions or for small-scale phenomena are primarily located in Region III. Because gas explosions are highly nonlinear, and the confinement level is not the only factor that determines blast load characteristics, load characteristics of some explosion scenarios might not be consistent with the aforementioned analysis. Nonetheless, it has been empirically confirmed that for both hydrocarbon and hydrogen explosions, as the confinement level increases, more severe blast loads are observed, and blast load characteristics could be classified and analyzed according to explosion conditions.

Figure 3 shows the correlations between peak overpressure and rising time-to-duration ratio for hydrocarbon and hydrogen explosions. The closer the x-axis value is to 0 or 1, the closer the blast load shape is to a right triangle, whereas the closer the x-axis value is to 0.5,

the closer the blast load shape is to an isosceles triangle. For hydrocarbon explosions, an inverse proportional trend between peak overpressure and rising time-to-duration ratio is observed. This indicates that as the peak overpressure of a blast increases, strain rates of a structure exposed to the blast load are also likely to increase because the rise time is shorter. For general steel grades, as the strain rate increases, fracture strain decreases, which could be disadvantageous from the perspective of the accidental limit state.

In the case of hydrogen explosions, on the other hand, the correlation is less consistent with a simple inverse proportionality. This is because blast load characteristics observed in experiments under low confinement conditions are located within the region with peak overpressures less than 0.2 MPa and rising time-to-duration ratios less than 0.2. Indeed, peak overpressures less than 0.2 MPa were observed in numerous hydrogen explosion experiments. Since these experiments might have been strongly influenced by uncontrolled experimental variables, which cause sensitively changing blast load characteristics, the trend of inverse proportionality would be weakened. If the experimental variables are sufficiently controlled and experiments observing blast loads with peak overpressures greater than 0.5 MPa are abundantly conducted, a more pronounced inversely proportional trend between the blast load characteristics could be expected to be observed.

Figure 4 shows nondimensionalized time-overpressure curves, visually presenting geometrical characteristics of hydrocarbon and hydrogen blast loads. Time and overpressure were nondimensionalized by rising time and peak overpressure, respectively. Therefore, all nondimensionalized curves pass through the (1, 1) coordinates. Because the large amount of experimental data precludes analysis of the geometrical characteristics, two curves representing the sharpest and most blunt cases (Min. and Max. t_d/t_r in Figure 4) and a single curve representing the mean of these two curves (Mean t_d/t_r in Figure 4) are presented. Similar blast load shapes were observed for the curves of minimum t_d/t_r, as the curves had similarly low peak overpressures of less than 0.02 MPa. However, except for the curves, the blast load shape of hydrogen explosions was closer to a right triangle than that of hydrocarbon explosions. This difference in load shape shows that an appropriate load model for hydrocarbon and hydrogen explosions should be applied in related simulations, particularly in structural response analysis.

3. Methods

3.1. Numerical Model for Dynamic Structural Response Analysis

A blast wall is a structure designed to prevent propagation of blast load and flame caused by an explosion to the surroundings. In this study, a corrugated blast wall, commonly installed in offshore structures with high explosion risks, was selected as a target structure and applied to numerical simulations. A blast wall is generally a site-specifically designed structure. However, since installation conditions for design did not exist, the intermediate section of design guidance for a corrugated blast wall provided by Louca and Boh [59] was adopted as dimensions of the target structure. The target structure consisted of corrugated panels and angle-type supports and was assumed to be made of duplex stainless steel 2205. A bilinear elasto-plastic model was applied as a material model, and nominal values of material properties were used in the material model to carry out simulations conservatively. The material properties used in the model are provided in Table 3.

The strain rate effect was considered by the Cowper–Symonds equation [60] as presented in Equation (1), and C of 100 and q of 4 were used as constants in the equation [61].

In this equation, σ_{Yd} and σ_Y are dynamic and static yield strengths, respectively, and $\dot{\varepsilon}$ is the strain rate.

$$\frac{\sigma_{Yd}}{\sigma_Y} = 1.0 + \left(\frac{\dot{\varepsilon}}{C}\right)^{1/q} \quad (1)$$

Table 3. Material properties used in the bilinear elasto-plastic model.

Material Properties	Duplex SS2205
Density	7.85×10^{-9} t/mm^3
Elastic modulus	210,000 MPa
Poisson's ratio	0.3
Yield strength	450 MPa
Tangent modulus	630 MPa
Fracture strain	0.3

To account for damping effects in a numerical simulation, a damping constant of $0.4\pi/T_N$ was used for all directional damping forces [23]. The T_N represents the natural period of the blast wall obtained from modal analysis. Surface-to-surface contact between the corrugated panel and the angle-type support, as well as single-surface contact on the corrugated panel, were defined to capture potential interactions between structural components. A static friction coefficient of 0.55 and a dynamic friction coefficient of 0.45 were used to define the contact conditions. These values represent the median values within the typical range for dry contact between clean stainless steel surfaces. Simply supported and symmetric boundary conditions were applied to the ends of supports and corrugated panels, respectively. For the blast load, a time-varying pressure was applied over the entire surface of the blast wall in the direction indicated by the red arrow (-Y direction) in Figure 5, without conducting separate Computational Fluid Dynamics (CFD) or Fluid-Structure Interaction (FSI) simulations. This time-varying pressure corresponds to the blast load scenario described in Section 3.2. four-node fully integrated shell elements were used in the numerical model, and the size of elements was determined based on existing literature [62] and the mesh convergence study presented in Figure 6. In the mesh convergence study, maximum and permanent displacements at the center of the corrugated blast wall were compared for different element sizes. Computation time was also compared due to the large number of simulations required. When the element size was set to 30 mm, the displacements converged while having a reasonable computation time. Therefore, an element size of 30 mm was determined for analyzing the dynamic structural response of the blast wall. The characteristic length used for time step calculation was defined as the element area divided by the maximum element edge length. Termination times were set to three times the blast load durations to observe complete structural responses, including the effect of inertia force. The blast load durations are described in detail in Section 3.2. An explicit solver in LS-DYNA was used for the simulations, employing the numerical model described previously and shown in Figure 5. The numerical model was entirely implemented by the authors, and no pre-defined numerical procedures provided by the software were utilized.

A validation of the numerical model was performed prior to simulations for blast load scenarios. The 1/4 scale test conducted by Schleyer and Langdon [63] was modeled numerically through the method described in the preceding paragraph, and predicted structural responses were compared with measured responses. Figure 7 compares the measured and predicted displacements at the mid-span of a central corrugation. The load applied to the simulation is also shown as a blue dash-dot line. A high level of agreement between the measured and predicted displacements was observed in terms of maximum displacement and overall response trends. However, a difference between measured

and predicted vibration periods was observed. This difference might be attributed to uncontrolled variables in the experiment, such as non-uniform load distribution and asymmetry of the test structure, which led to relatively non-ideal structural response and more complex deformation modes compared with the simulation.

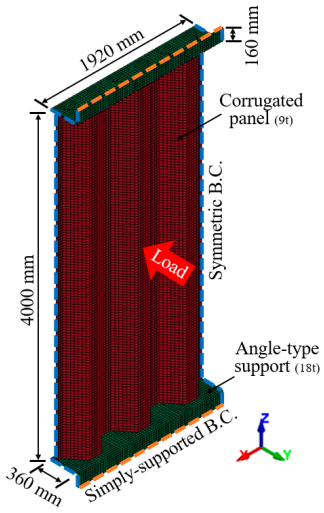


Figure 5. Numerical model of the corrugated blast wall.

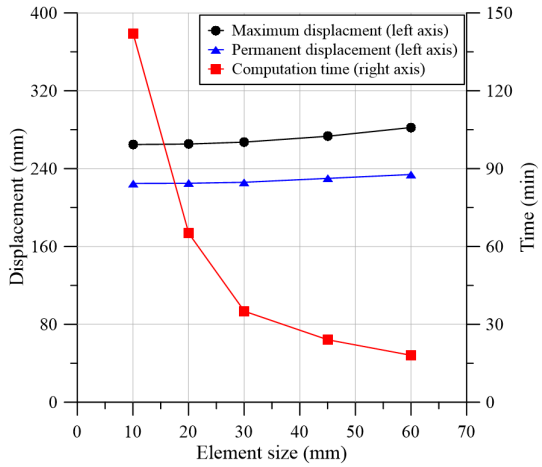


Figure 6. Mesh convergence study of maximum and permanent displacements and computation time for the dynamic structural analysis of corrugated blast wall.

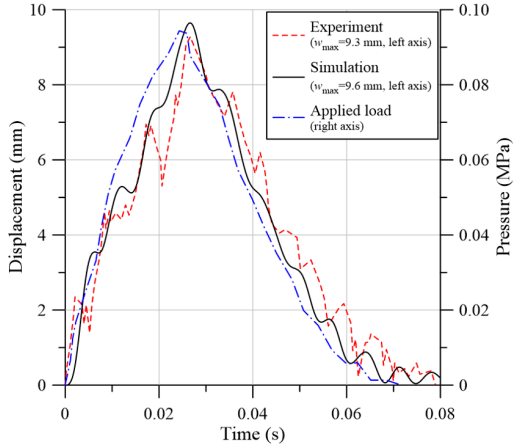


Figure 7. Validation of the numerical model using experimental data: comparison of time-displacement curves at the mid-span.

Figure 8a,b compares deformed shapes of the overall panel and connection, respectively. For the overall panel, both the experiment and the simulation showed structural responses reflecting anisotropic geometric characteristics of the corrugated blast wall. Moreover, greater deflections were observed toward the mid-span due to the influence of boundary conditions and local buckling. The connection is designed to unfold after blast loading, allowing blast walls to efficiently absorb impact energies. In both the experiment and the simulation, the connection deformed into a similar shape after being loaded, consistent with its intended function. In these comparisons, a high level of agreement between the measured and predicted structural responses was observed, confirming the validity of the numerical model.

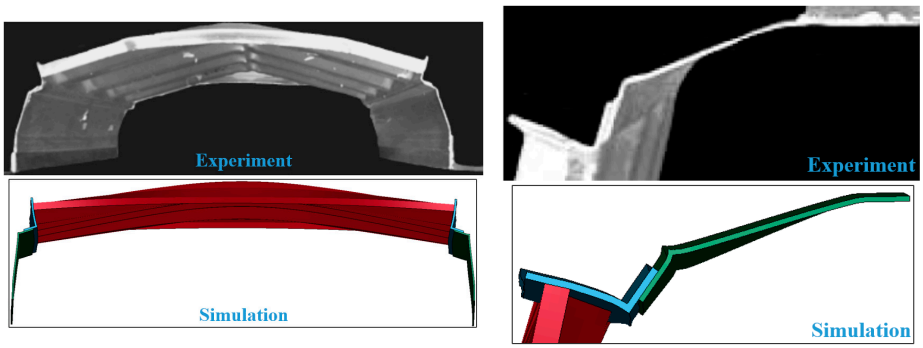
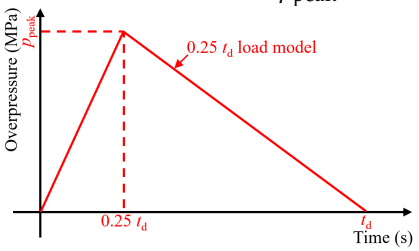


Figure 8. Validation of the numerical model using experimental data: comparison of deformations for (**a**) overall panel and (**b**) connection.

3.2. Blast Load Scenarios of Hydrogen and Hydrocarbon Explosions

Blast load scenarios were selected based on the blast load characteristics analyzed in the preceding section and prior research. Dynamic structural response of the target structure was observed in numerical simulations of these scenarios. The blast load scenarios are summarized in Table 4. The peak overpressure for hydrocarbons was determined by referencing the nominal blast overpressure provided by API [64]. The peak overpressure for hydrogen was determined based on the observed characteristic that the maximum peak overpressure (Max. p_{peak}) in Figure 1b was approximately 3.5 times greater than that of hydrocarbons. The duration was initially determined as the range in which the dynamic response caused by inertial force was observed [65,66], through a parametric study. Peak overpressure and duration were assumed to be independent, and all combinations of these two load characteristics were included in the scenarios. This assumption was justified by the blast load characteristics that, even for explosions with a similar level of peak overpressure, different durations can be observed depending on other explosion conditions, as shown in Figure 2. The inversely proportional trend between peak overpressure and rising time-to-duration ratio observed in Figure 3 was also considered in the blast load scenarios. Accordingly, load models for each peak overpressure are summarized in the fourth row of Table 4. The $0.25t_d$ model represents the triangular impulse load with a rising time-to-duration ratio of 0.25. A visual example of this model is provided in the fifth row of Table 4. As a result, 40 and 130 blast load scenarios were selected for hydrocarbon and hydrogen explosions, respectively.

Table 4. Blast load scenarios for hydrocarbon and hydrogen explosions.

	Hydrocarbon	Hydrogen
Peak overpressure (p_{peak})	0.05/0.1/0.2/0.3 MPa	0.05/0.1/0.2/0.3/0.4/0.5/0.6/0.7/ 0.8/0.9/1.0/1.1/1.2 MPa
Duration (t_d)	0.01/0.02/0.03/0.04/0.06/0.08/0.10/0.13/0.16/0.20 s	
Load model	p_{peak} of 0.05–0.1 MPa: $0.75t_d$ model p_{peak} of 0.2 MPa: $0.50t_d$ model p_{peak} of 0.3 MPa: $0.25t_d$ model	p_{peak} of 0.05–0.1 MPa: $0.75t_d$ model p_{peak} of 0.2 MPa: $0.50t_d$ model p_{peak} of 0.3–0.5 MPa: $0.25t_d$ model p_{peak} of 0.6–1.2 MPa: $0.00t_d$ model
Example of load model		
Number of scenarios	40 (4 peak overpressures × 10 durations)	130 (13 peak overpressures × 10 durations)

In the following section, the dynamic structural response of the blast wall was analyzed from the perspective of maximum and permanent y-displacements at the mid-span of the blast wall (*Disp.*$_{maximum}$ and *Disp.*$_{permanent}$) and maximum and residual strain energies of the corrugated panel (*S.E.*$_{maximum}$ and *S.E.*$_{residual}$). For clarity, Figure 9 shows y-displacement at the mid-span and strain energy of the corrugated panel in the blast load scenario with peak overpressure of 0.5 MPa and duration of 0.1 s. In addition, it presents the definitions of the maximum and permanent y-displacements, as well as the maximum and residual strain energies.

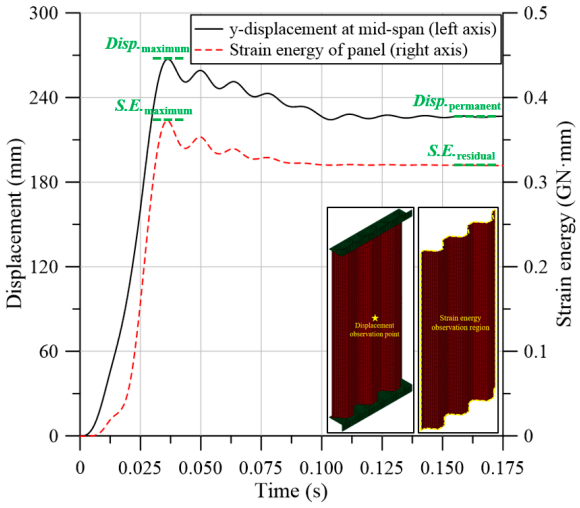


Figure 9. Definitions of maximum and permanent displacements and maximum and residual strain energies.

4. Results

Figure 10 shows the maximum and permanent displacements at the mid-span for all blast load scenarios. The x-axis presents durations nondimensionalized by the natural period (T_N) for each scenario. As the peak overpressure increased, the maximum displacement also increased, but the increasing trends over duration depended on the

level of peak overpressure. For load scenarios with peak overpressures of 0.1 MPa or less, because elastic deformation occurred at the corrugated panel and supports, the resonance between blast load and structure acted as a significant factor in determining structural response. Therefore, the greatest deformation was observed around a t_d/T_N of 1. In blast load scenarios with peak overpressures of 0.2–0.3 MPa, plastic deformation at the supports spread to the corrugated panel, and the stiffness of the blast wall therefore decreased. This decrease in stiffness elongated the natural period of the blast wall [67,68], and, thus, the greatest structural deformation was observed after t_d/T_N of 1.

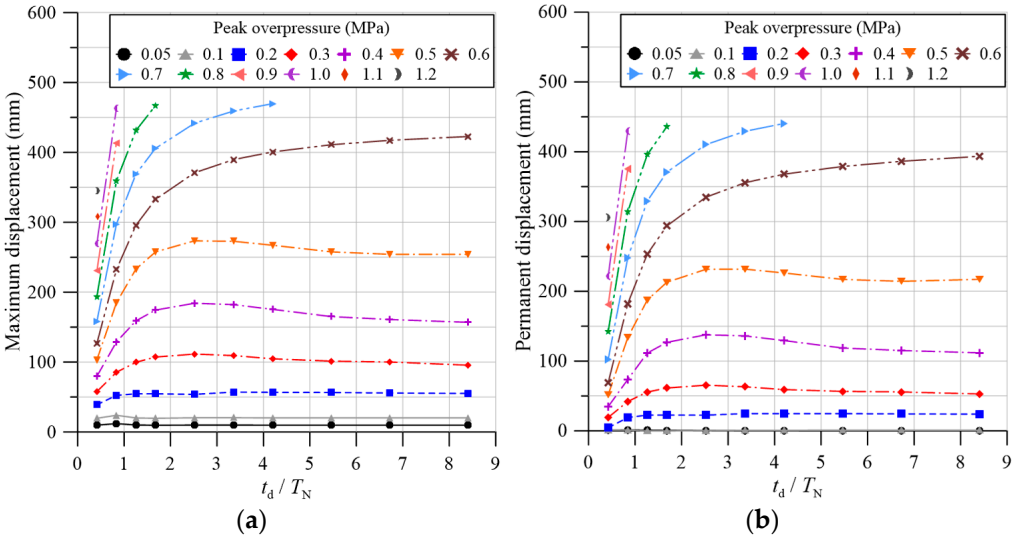


Figure 10. Dynamic structural responses depending on nondimensionalized time and peak overpressure: (**a**) maximum and (**b**) permanent displacements at the mid-span.

When peak overpressures are 0.4 MPa or greater, all load scenarios correspond to only hydrogen explosions. In these scenarios, when the peak overpressure increased by 0.1 MPa, the maximum and permanent displacements increased more rapidly than in the hydrocarbon load scenarios. This indicated that plastic deformation occurred throughout the blast wall and rapidly increased. In the case of corrugated blast walls with angle-type supports, plastic deformation generally occurs first in the supports and then in the panel. This sequential relationship could be confirmed by the permanent displacement and residual strain energy diagrams. In load scenarios with a peak overpressure of 0.2 MPa, the strain energies at the corrugated panel were so insignificant and did not remain permanently. However, permanent displacements at the mid-span began to be observed because plastic deformation occurred at the supports.

Figure 11 presents the maximum and residual strain energies of the corrugated panel for all blast load scenarios. Increasing trends in both the maximum and residual strain energies were observed with higher peak overpressures. This trend indicates that larger deformations occurred in the panel as the peak overpressure increased. From blast load scenarios with a peak overpressure of 0.3 MPa, the maximum strain energy increased significantly, and the residual strain energy began to appear. The presence of residual strain energy demonstrates that plastic deformation occurred in the corrugated panel. Residual strain energies became more pronounced in blast load scenarios with peak overpressures of 0.4 MPa or greater. This suggests that the panel is likely to absorb a greater portion of blast loads under such loading conditions.

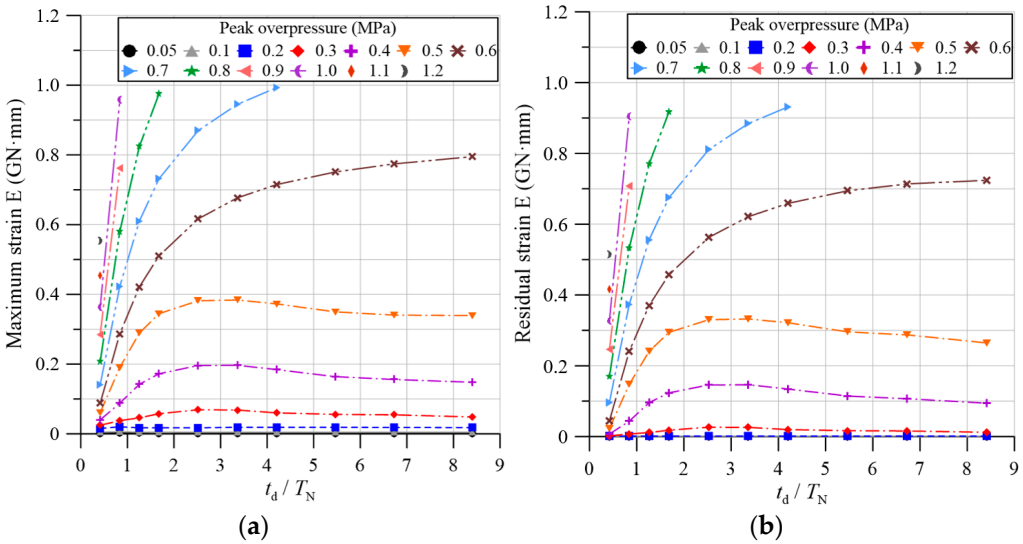


Figure 11. Dynamic structural responses depending on nondimensionalized time and peak overpressure: (**a**) maximum and (**b**) residual strain energies of corrugated panel.

In blast load scenarios with peak overpressures of 0.6 MPa or greater, plastic deformation at the corrugated panel rapidly increased, causing large deformations of the entire blast wall. No resonances between the blast load and natural period were observed because of the significant decrease in structural stiffness caused by large deformations. A localized or global fracture was observed in certain load scenarios with peak overpressures of 0.7 MPa or greater. As blast walls with even the slightest fracture could be considered to be in a failure state, these cases are not plotted in Figures 10 and 11, corresponding to the part beyond the cut curves in these figures. As the peak overpressure increased, the duration necessary to cause a fracture shortened increasingly. At peak overpressures of 1.6 MPa or greater, fractures were observed regardless of duration. Moreover, a deflection exceeding the recommended deflection limits for blast walls provided by FABIG [69] was observed in the blast load scenario with a peak overpressure of 0.5 MPa. This excessive deflection shows the potential difficulty of sufficiently responding to hydrogen explosion accidents with a corrugated blast wall designed for hydrocarbon fuels.

The P–I diagram and the resistance curve, briefly mentioned earlier, are representative tools typically employed for the structural response analysis of blast walls. While these tools have long been utilized as powerful tools in blast wall design, they exhibit the following limitations: First, both the diagram and the curve present only a single structural response (usually the maximum displacement of the blast wall) for a given blast load, making it difficult to assess localized failures. Individually, the P–I diagram presents multiple iso-damage curves; however, drawing these curves requires a substantial number of simulations. Since performing such simulations using the Finite Element Method (FEM) is computationally inefficient, the Single Degree of Freedom (SDOF) method is generally adopted to predict the structural response, which could reduce the validity of the iso-damage curves. Moreover, highly unrealistic blast load scenarios might be included in the diagram to draw the curves. Although the resistance curve provides a more intuitive representation of structural response by presenting displacement under applied loads, it is generally derived for specific loading conditions, such as static loads or nominal blast loads. Consequently, its applicability becomes limited in hydrogen explosions, which could involve highly nonlinear structural responses of blast walls.

To overcome these limitations, a new type of diagram was proposed in this study. Figure 12 illustrates the proposed diagram, which integrates the structural responses analyzed in the previous paragraphs. The x-axis presents the ratio between the residual

and maximum strain energies that occurred at the corrugated panel, and the y-axis presents the ratio between the permanent and maximum displacements at the mid-span of the target structure. Each data point represents the dynamic structural response characteristics for a single blast load scenario. This diagram is similar to the resistance curve but has the advantages of including the structural response for diverse blast load scenarios and enabling assessment of the degree of damage in a specific structural member. The analysis based on this diagram is as follows. In the case of load scenarios with peak overpressures of 0.2 MPa or less, plastic deformation mostly occurred at supports, and a linearly proportional trend between the ratios was observed. When the peak overpressure increased to 0.3 MPa, plastic deformation at the corrugated panel began to occur in earnest, and all blast load scenarios for hydrocarbon were exhausted. A trend in which plastic deformations of the panel and supports increased nonlinearly was observed in blast load scenarios with peak overpressures of 0.4 MPa or greater. In this stage of structural response, the blast loads absorbed by the corrugated panel increased significantly. However, when the peak overpressure reached 0.5 MPa, it was observed that the plastic deformations of the panel and supports increased together. Ultimately, this significant increase led to fracture and structural collapse of the target structure.

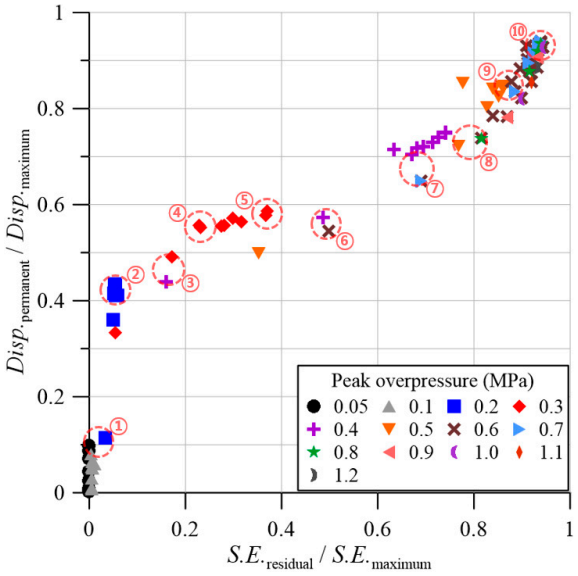


Figure 12. The ratio of residual strain energy to maximum strain energy—the ratio of permanent displacement to maximum displacement diagram.

Figure 13a–c present the von Mises stress (left column) and effective plastic strain (right column) distributions at the moment when the blast wall reaches its maximum displacement for locations ②, ⑥, and ⑨ in Figure 12, respectively. These locations represent initial, intermediate, and final sections of the strain energy ratio-displacement ratio diagram, respectively. This figure shows regions of the blast wall where equivalent stress and plastic strain occurred, with redder areas indicating relatively larger deformation at those points compared with the surrounding areas. The distributions and deformed shapes exhibited a trend consistent with the analysis derived from the strain energy ratio-displacement ratio diagram. However, in the blast load scenario for location ②, in which little plastic deformation occurred in the corrugated panel, plastic deformation was observed at joints between the supports and panel as well as the supports. This was because the target structure had geometrical features that could cause stress concentration at the joints.

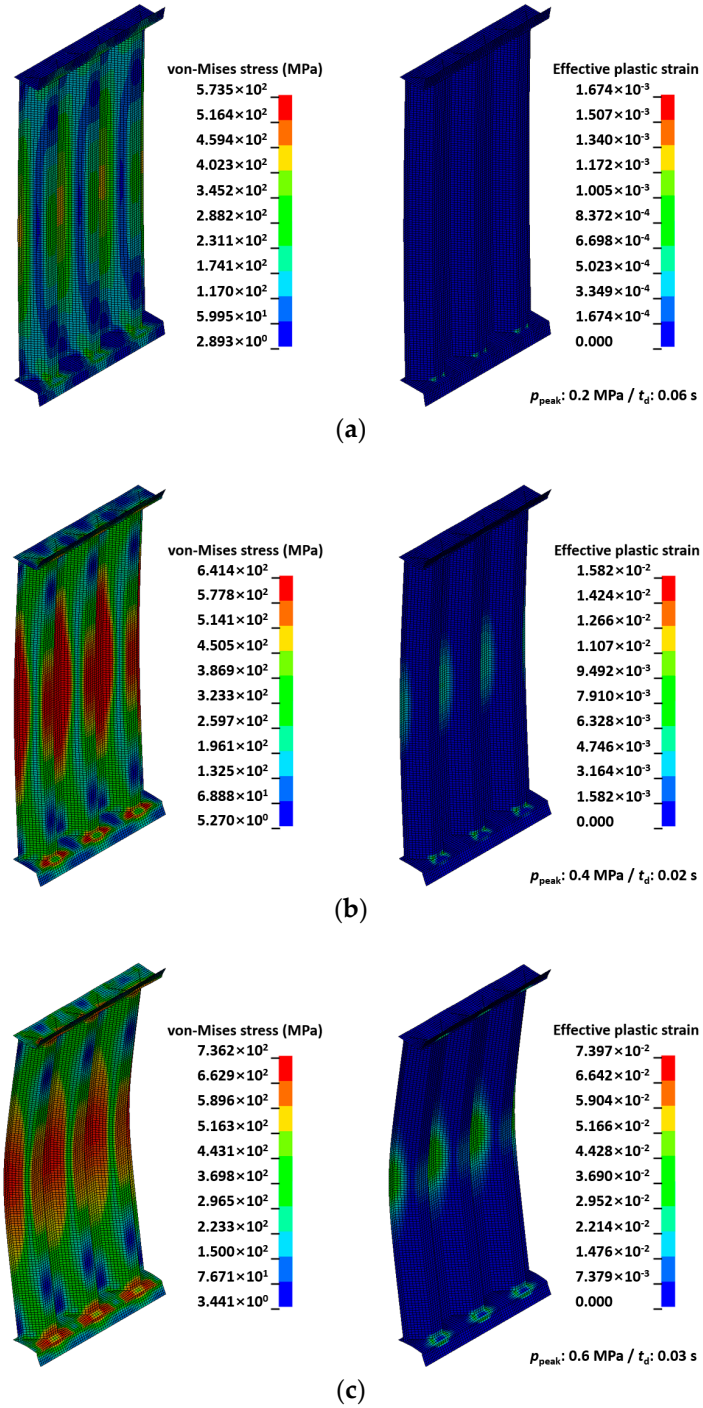


Figure 13. von Mises stress and effective plastic strain distributions for (**a**) location ②, (**b**) location ⑥, and (**c**) location ⑨.

Figure 14a–c present time-series strain energies that occurred at the panel and support for the locations ②, ⑥, and ⑨, respectively. The load applied to blast walls is also shown as a black solid line. This figure shows which structural component primarily absorbs the applied load. In the blast load scenario for location ②, the maximum strain energy of the support was greater than that of the panel, indicating that the support contributed more to absorbing the blast load compared with the panel. Moreover, most of the residual strain energy was observed in the support. This was because shape differences between the support and the panel caused large deformations to occur earlier in the support. In the blast load scenario for location ⑥, the maximum strain energy of the panel increased to a

level comparable to that of the support. In addition, it was observed that the residual strain energy of the panel increased significantly. This increase indicates that location ⑥ is a stage where the contribution of the panel to blast load absorption becomes more significant. In the blast load scenario for location ⑨, unlike the previous locations, the relationship between the strain energies of the panel and support was completely reversed. At this location, significant plastic deformation occurs in the panel, allowing the blast wall to absorb high-intensity blast loads. However, maximum and residual strain energies of both the panel and the support were observed to be at similar levels for each structural member. This suggests that both the structural members have almost lost their ability to recover, and the blast wall is approaching structural collapse.

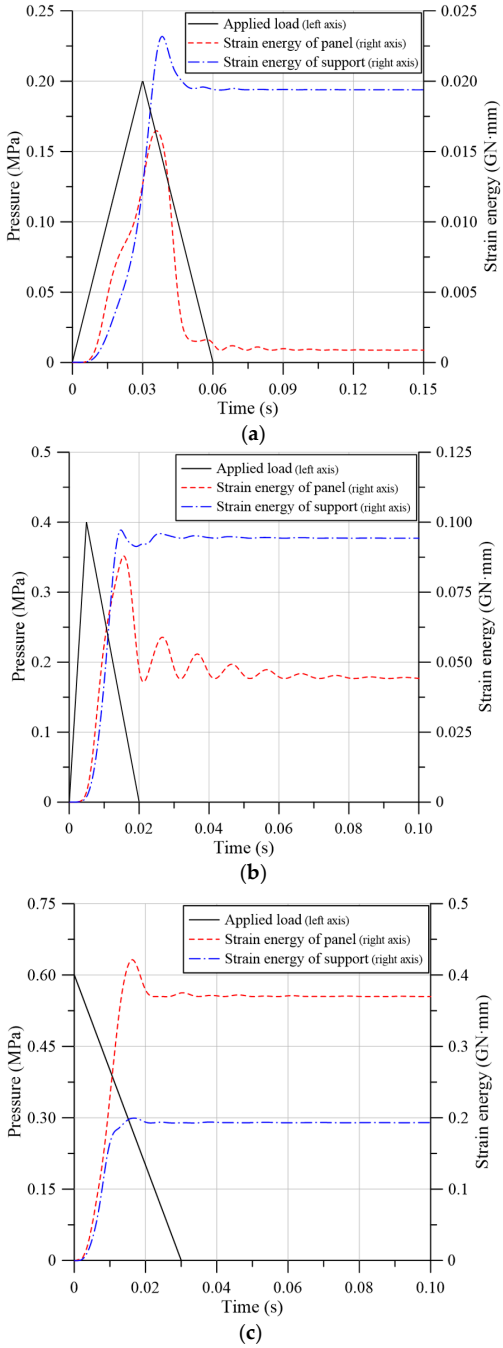


Figure 14. Applied load and time-strain energy curves for (**a**) location ②, (**b**) location ⑥, and (**c**) location ⑨.

In addition to the previous analyses, deformation modes of corrugated blast walls were defined by the quantitative structural response at all locations indicated by dotted circles and numbering in Figure 12. Figure 15 presents maximum effective plastic strains at the mid-span of the corrugated panel and strain energies of the entire blast wall for each location. Modes I and II were distinguished by whether or not plastic deformation occurred at the corrugated panel mid-span. The occurrence of plastic deformation at the mid-span could indicate the starting point for large deformation of the corrugated panel. The plastic deformation was observed for the locations ③ and above. Modes II and III were distinguished based on the maximum strain energy, which could be regarded as a measure of the deformation throughout the blast wall. The maximum strain energy increased relatively linearly up to location ⑦ but began to increase nonlinearly from location ⑧. This nonlinearity could indicate that the level of deformation throughout the blast wall increases rapidly. Therefore, location ⑧ was determined as the start of Mode III.

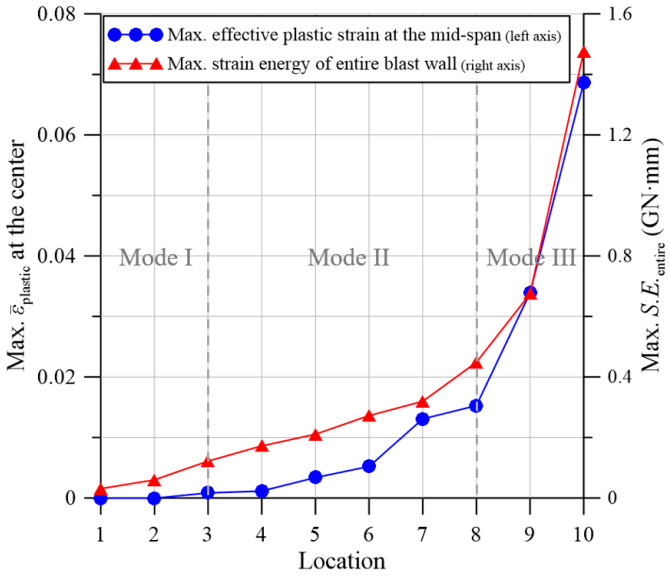


Figure 15. Maximum effective plastic strain and global strain energy at each location.

Consequently, deformation modes were determined as shown in Figure 16. In order to clearly divide the distribution of the overall upward-trending data, boundaries were drawn as straight lines passing through the (0,1) coordinate and the blast load scenario that satisfied the criteria in Figure 15 and was closest to the origin. In Mode I, named support yielding, deformation occurs throughout the blast wall, but plastic deformation is mostly observed at supports and joints between the supports and panel. In Mode II, named panel yielding, a rapid increase in plastic deformation at a corrugated panel is observed after severe deformation has occurred at the supports and joints. Lastly, in Mode III, named overall collapse, plastic deformation throughout the corrugated blast wall increases drastically. Therefore, the possibility of fracture and structural collapse also increases significantly. For hydrocarbon explosions, most blast load scenarios corresponded to Mode I, with some severe scenarios classified as Mode II. However, hydrogen blast load scenarios were observed in all three modes, with a large proportion of scenarios classified as Mode III. These results show the risk of hydrogen explosions from a structural perspective.

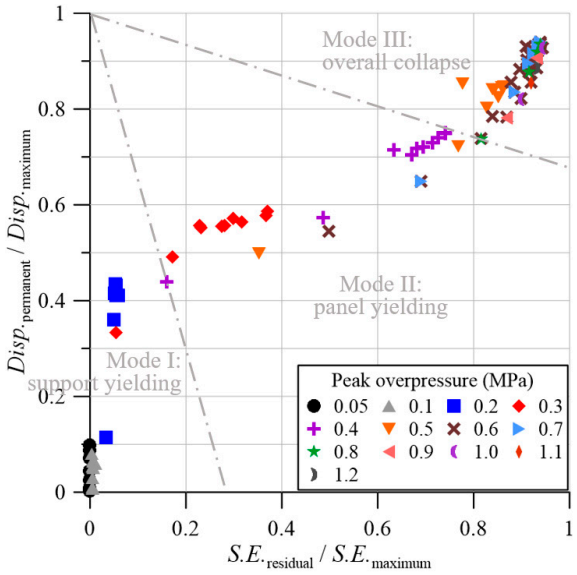


Figure 16. Deformation modes of corrugated blast wall under hydrogen blast loads.

5. Discussion and Conclusions

A comprehensive literature review was conducted on studies that carried out explosion experiments to analyze and compare blast load characteristics of hydrocarbons and hydrogen, and the following results were observed: Hydrogen explosions tended to have greater peak overpressure and shorter duration than hydrocarbon explosions. As the confinement level of explosion spaces increased, the blast load became more severe. An inversely proportional trend between peak overpressure and rising time-to-duration ratio was observed, except for some experiments conducted in spaces with low confinement levels.

The aforementioned blast load characteristics are partially consistent with commonly accepted trends in gas explosion characteristics. However, studies that have empirically validated these trends are limited, and those that have directly compared the load characteristics of hydrocarbon and hydrogen explosions are extremely rare. Therefore, the blast load characteristics analyzed in this study might serve as valuable empirical references for the development of safety rules, design standards, and blast load scenarios for hydrogen fuels. If future analyses include a broader range of large-scale explosion experiments and consider the negative phase of blast loads, hydrogen blast load characteristics will be more clearly investigated.

Blast load scenarios were selected on the basis of the analyzed blast load characteristics, and the dynamic structural response of a corrugated blast wall was investigated by applying these scenarios to numerical simulations. The blast load scenarios were applied as time-varying pressures over the entire surface of the blast wall. This method offers both practicality and reasonable accuracy when a large number of scenarios need to be analyzed. However, it also involves a certain degree of blast load idealization compared with CFD or FSI simulations. The following results were observed from the numerical simulations: when relatively weak peak overpressures were applied, the blast wall behaved quasi-elastically, and the maximum dynamic structural response was observed around t_d/T_N of 1 because of the resonance between the blast load and the natural period of the blast wall. However, as the peak overpressure increased and the area of plastic deformation widened, the maximum dynamic structural response was observed in the region of t_d/T_N higher than 1. Moreover, deflection exceeding the recommended deflection limits and localized fracture were observed in hydrogen blast load scenarios with peak overpressures of 0.5 and 0.7 MPa, respectively.

The structural responses described in the preceding paragraph demonstrated that the impulse of blast loads and the deformation of blast walls might not be proportional in load scenarios with relatively low peak overpressures, where elastic deformation primarily occurred. Therefore, the P–I diagram, commonly used in the design of blast walls, could be appropriately drawn after some degree of plastic deformation has occurred in the wall. It was observed that the deformation of the blast wall exceeded recommended deflection limits from the blast load scenario with a peak overpressure of 0.5 MPa. This indicates that it is insufficient to block hydrogen blast loads with high peak overpressures, although the existing blast wall is capable of resisting hydrocarbon explosions as intended. Fracture was initiated at the connection between the corrugated panel and the support, as shown by the von Mises stress and plastic strain distributions. This phenomenon highlights that the structural integrity of blast walls depends not only on the panel design but also on the appropriate design of the support and its connection.

A new type of diagram for structural response analysis of corrugated blast walls was proposed. Furthermore, three deformation modes of a corrugated blast wall were defined on the proposed diagram based on qualitative and quantitative structural responses. The diagram is similar to a resistance curve but has the additional advantages of covering diverse blast load scenarios and enabling assessment of the degree of damage in a specific structural member. In this study, the diagram was constructed using the displacement at the center of the blast wall and the strain energy of the corrugated panel. However, it could also be extended by substituting the strain energy of the panel with that of another structural member or even by constructing the diagram using only the strain energies of structural members without utilizing displacement data. Moreover, this diagram might be applicable to other types of blast walls or to structures composed of multiple structural members.

These findings provide a fundamental basis for advancing the design and evaluation of structural systems subjected to hydrogen blast loads.

Author Contributions: Conceptualization, H.L. and J.S.; methodology, H.L. and J.S.; software, H.L.; validation, H.L.; formal analysis, H.L. and J.S.; investigation, H.L. and J.S.; resources, J.S.; data curation, H.L.; writing—original draft preparation, H.L.; writing—review and editing, H.L.; visualization, H.L.; supervision, J.S.; project administration, J.S.; funding acquisition, J.S. All authors have read and agreed to the published version of the manuscript.

Funding: This work was supported by the National Research Foundation of Korea (NRF) grant funded by the Korea government (MSIT) (No. RS-2024-00348014).

Institutional Review Board Statement: Not applicable.

Informed Consent Statement: Not applicable.

Data Availability Statement: The simulation data generated in this study are freely accessible for research purposes only. Experimental data cited in this paper were obtained from previously published studies, which are listed in the references.

Conflicts of Interest: The authors declare no conflicts of interest.

References

1. International Maritime Organization (IMO). *ANNEX 15: 2023 IMO Strategy on Reduction of GHG Emissions from Ships*; IMO: London, UK, 2023.
2. Law, L.C.; Foscoli, B.; Mastorakos, E.; Evans, S. A Comparison of Alternative Fuels for Shipping in Terms of Lifecycle Energy and Cost. *Energies* **2021**, *14*, 8502. [CrossRef]
3. Marchuk, A.; Likhanov, V.A.; Lopatin, O.P. Alternative energy: Methanol, ethanol and alcohol esters of rapeseed oil as eco-friendly biofuel. *Theor. Appl. Ecol.* **2019**, *3*, 80–86. [CrossRef]
4. Sangeeta; Moka, S.; Pande, M.; Rani, M.; Gakhar, R.; Sharma, M.; Rani, J.; Bhaskarwar, A.N. Alternative fuels: An overview of current trends and scope for future. *Renew. Sustain. Energy Rev.* **2014**, *32*, 697–712. [CrossRef]

5. Lee, Y.; Cho, M.H.; Lee, M.C.; Kim, Y.J. Evaluating hydrogen risk management policy PR: Lessons learned from three hydrogen accidents in South Korea. *Int. J. Hydrogen Energy* **2023**, *48*, 24536–24547. [CrossRef]
6. Hansen, O.R. Hydrogen infrastructure-Efficient risk assessment and design optimization approach to ensure safe and practical solutions. *Process Saf. Environ. Prot.* **2020**, *143*, 164–176. [CrossRef]
7. Mo, L.; Wang, R.; Yang, H.; Yang, Y.; Wu, X.; Jia, W.; Li, C.; Chen, C. Dynamic response of spherical tanks subjected to the explosion of hydrogen-blended natural gas. *Fuel* **2024**, *377*, 132834. [CrossRef]
8. Wang, J.; Liang, Z.; Lin, J.; Feng, H.; Zhang, S. Structural response for vented hydrogen-air deflagrations: Effects of volumetric blockage ratio. *Process Saf. Prog.* **2023**, *43*, 284–292. [CrossRef]
9. Haghgoo, M.; Babaei, H.; Mostofi, T.M. Numerical simulation of the influence of confined multi-point ignited H_2–O_2 mixture on the propagation of shock waves towards a deformable plate. *Int. J. Hydrogen Energy* **2022**, *47*, 27080–27095. [CrossRef]
10. Hao, T.; Wang, C.; Yan, W.; Ren, W.; Yuen, K. Experimental investigation on the dynamic responses of vented hydrogen explosion in a 40-foot container. *Int. J. Hydrogen Energy* **2021**, *46*, 19229–19243. [CrossRef]
11. Du, Y.; Zhou, F.; Zheng, L.; Hu, W.; Liao, B.; Ma, L.; Zheng, J. Comparison of mode-I crack propagation of tube subjected to internal hydrogen static and detonation loading. *Int. J. Hydrogen Energy* **2020**, *45*, 11199–11210. [CrossRef]
12. Russo, P.; De Marco, A.; Parisi, F. Assessment of the Damage from Hydrogen Pipeline Explosions on People and Buildings. *Energies* **2020**, *13*, 5051. [CrossRef]
13. Liu, F.; Wang, Z.; Cao, X.; Guo, P.; Lu, Y.; Xiao, J.; Qian, Y. Experimental investigation on the dynamic reactions of concrete walls coated with blast-resistant materials to hydrogen explosions. *Int. J. Hydrogen Energy* **2025**, *142*, 490–497. [CrossRef]
14. Du, Y.; Liu, Y.; Zhou, F.; Li, Z.; Ma, L.; Liu, B. Evaluation of blast wave from hydrogen pipeline burst by a coupled fluid-structure-rupture approach. *Int. J. Hydrogen Energy* **2024**, *55*, 696–703. [CrossRef]
15. Myilsamy, D.; Oh, C.B.; Kim, K.S. Numerical study on blast wall configurations on pressure behavior in high-pressure hydrogen tank explosions. *Int. J. Hydrogen Energy* **2024**, *93*, 1071–1087. [CrossRef]
16. Go, G.H.; Cao, V.H.; Kim, Y.; Choi, H.; Oh, S.W.; Kim, M.J. Evaluation of the Dynamic Stability of Underground Structures Assuming a Hydrogen Gas Explosion Disaster in a Shallow Underground Hydrogen Storage Facility. *Appl. Sci.* **2023**, *13*, 12317. [CrossRef]
17. Signetti, S.; Klomfass, A.; Riedel, W.; Putzar, R.; Heine, A. Simulation of blast propagation and structural effects of accidental hydrogen-air-mixture explosion in a two-stage light-gas gun laboratory for hypervelocity impact experiments. *J. Loss Prev. Process Ind.* **2023**, *85*, 105138. [CrossRef]
18. Wang, X.; Li, B.; Han, B.; Jin, X.; Zhang, D.; Bi, M. Explosion of high pressure hydrogen tank in fire: Mechanism, criterion, and consequence assessment. *J. Energy Storage* **2023**, *72*, 108455. [CrossRef]
19. Bratland, M.; Bjerketvedt, D.; Vaagsaether, K. Structural response analysis of explosions in hydrogen-air mixtures in tunnel-like geometries. *Eng. Struct.* **2021**, *231*, 111844. [CrossRef]
20. Atanga, G.; Lakshmipathy, S.; Skjold, T.; Hisken, H.; Hanssen, A.G. Structural response for vented hydrogen deflagrations: Coupling CFD and FE tools. *Int. J. Hydrogen Energy* **2019**, *44*, 8893–8903. [CrossRef]
21. Shepherd, J.E. Structural response of piping to internal gas detonation. *J. Press. Vessel Technol.* **2009**, *131*, 031204. [CrossRef]
22. Krieg, R.; Dolensky, B.; Göller, B.; Breitung, W.; Redlinger, R.; Royl, P. Assessment of the load-carrying capacities of a spherical pressurized water reactor steel containment under a postulated hydrogen detonation. *Nucl. Technol.* **2003**, *141*, 109–121. [CrossRef]
23. Livermore Software Technology Corporation (LSTC). *LS-DYNA Keyworkd User's Manual: Volume I*; LSTC: Livermore, CA, USA, 2018.
24. Sato, Y.; Iwabuchi, H.; Groethe, M.; Merilo, E.; Chiba, S. Experiments on hydrogen deflagration. *J. Power Sources* **2006**, *159*, 144–148. [CrossRef]
25. Ferrara, G.; Willacy, S.K.; Phylaktou, H.N.; Andrews, G.E.; Di Benedetto, A.; Salzano, E.; Russo, G. Venting of gas explosion through relief ducts: Interaction between internal and external explosions. *J. Hazard. Mater.* **2008**, *155*, 358–368. [CrossRef] [PubMed]
26. Bauwens, C.R.; Chaffee, J.; Dorofeev, S.B. Vented explosion overpressures from combustion of hydrogen and hydrocarbon mixtures. *Int. J. Hydrogen Energy* **2011**, *36*, 2329–2336. [CrossRef]
27. Zhang, B.; Xiu, G.; Bai, C. Explosion characteristics of argon/nitrogen diluted natural gas-air mixtures. *Fuel* **2014**, *124*, 125–132. [CrossRef]
28. Li, G.; Wang, X.; Xu, H.; Liu, Y.; Zhang, H. Experimental study on explosion characteristics of ethanol gasoline-air mixture and its mitigation using heptafluoropropane. *J. Hazard. Mater.* **2019**, *378*, 120711. [CrossRef] [PubMed]
29. Shirvill, L.C.; Roberts, T.A.; Royle, M.; Willoughby, D.B.; Sathiah, P. Experimental study of hydrogen explosion in repeated pipe congestion-Part 2: Effects of increase in hydrogen concentration in hydrogen-methane-air mixture. *Int. J. Hydrogen Energy* **2019**, *44*, 3264–3276. [CrossRef]
30. Luo, Z.; Hao, Q.; Wang, T.; Li, R.; Cheng, F.; Deng, J. Experimental study on the deflagration characteristics of methane-ethane mixtures in a closed duct. *Fuel* **2020**, *259*, 116295. [CrossRef]

31. Li, G.; Wu, J.; Wang, S.; Bai, J.; Wu, D.; Qi, S. Effects of gas concentration and obstacle location on overpressure and flame propagation characteristics of hydrocarbon fuel-air explosion in a semi-confined pipe. *Fuel* **2021**, *285*, 119268. [CrossRef]
32. Li, Z.; Chen, L.; Yan, H.; Fang, Q.; Zhang, Y.; Xiang, H.; Liu, Y.; Wang, S. Gas explosions of methane-air mixtures in a large-scale tube. *Fuel* **2021**, *285*, 119239. [CrossRef]
33. Wakabayashi, K.; Mogi, T.; Kim, D.; Abe, T.; Ishikawa, K.; Kuroda, E.; Matsumura, T.; Nakayama, Y.; Horiguchi, S.; Oya, M. A Field Explosion Test of Hydrogen-Air Mixtures. In Proceedings of the 1st International Conference on Hydrogen Safety, Pisa, Italy, 8–10 September 2005.
34. Schneider, H. Large Scale Experiments-Deflagration and Deflagration to Detonation within a Partial Confinement Similar to a Lane. In Proceedings of the 1st International Conference on Hydrogen Safety, Pisa, Italy, 8–10 September 2005.
35. Middha, P.; Hansen, O.R.; Groethe, M.; Arntzen, B.J. Hydrogen Explosion Study in a Confined Tube: FLACS CFD Simulations and Experiments. In Proceedings of the 21st International Colloquium of Dynamics of Explosions and Reactive Systems, Poitiers, France, 23–27 July 2007.
36. Groethe, M.; Merilo, E.; Colton, J.; Chiba, S.; Sato, Y.; Iwabuchi, H. Large-scale hydrogen deflagrations and detonations. *Int. J. Hydrogen Energy* **2007**, *32*, 2125–2133. [CrossRef]
37. Makarov, D.; Verbecke, F.; Molkov, V.; Roe, O.; Skotenne, M.; Kotchourko, A.; Lelyakin, A.; Yanez, J.; Hansen, O.; Middha, P. An inter-comparison exercise on CFD model capabilities to predict a hydrogen explosion in a simulated vehicle refuelling environment. *Int. J. Hydrogen Energy* **2009**, *34*, 2800–2814. [CrossRef]
38. Bauwens, C.R.; Chao, J.; Dorofeev, S.B. Effect of hydrogen concentration on vented explosion overpressures from lean hydrogen-air deflagrations. *Int. J. Hydrogen Energy* **2012**, *37*, 17599–17605. [CrossRef]
39. Emami, S.D.; Rajabi, M.; Che Hassan, C.R.; Hamid, M.D.A.; Kasmani, R.M.; Mazangi, M. Experimental study on premixed hydrogen/air and hydrogen-methane/air mixtures explosion in 90 degree bend pipeline. *Int. J. Hydrogen Energy* **2013**, *38*, 14115–14120. [CrossRef]
40. Kim, W.K.; Mogi, T.; Dobashi, R. Fundamental study on accidental explosion behavior of hydrogen-air mixtures in an open space. *Int. J. Hydrogen Energy* **2013**, *38*, 8024–8029. [CrossRef]
41. Ma, Q.; Zhang, Q.; Chen, J.; Huang, Y.; Shi, Y. Effects of hydrogen on combustion characteristics of methane in air. *Int. J. Hydrogen Energy* **2014**, *39*, 11291–11298. [CrossRef]
42. Pang, L.; Wang, C.; Han, M.; Xu, Z. A study on the characteristics of the deflagration of hydrogen-air mixture under the effect of a mesh aluminum alloy. *J. Hazard. Mater.* **2015**, *299*, 174–180. [CrossRef] [PubMed]
43. Guo, J.; Li, Q.; Chen, D.; Hu, K.; Shao, K.; Guo, C.; Wang, C. Effect of burst pressure on vented hydrogen-air explosion in a cylindrical vessel. *Int. J. Hydrogen Energy* **2015**, *40*, 6478–6486. [CrossRef]
44. Kuznetsov, M.; Friedrich, A.; Stern, G.; Kotchourko, N.; Jallais, S.; L'Hostis, B. Medium-scale experiments on vented hydrogen deflagration. *J. Loss Prev. Process Ind.* **2015**, *36*, 416–428. [CrossRef]
45. Cao, Y.; Guo, J.; Hu, K.; Xie, L.; Li, B. Effect of ignition location on external explosion in hydrogen-air explosion venting. *Int. J. Hydrogen Energy* **2017**, *42*, 10547–10554. [CrossRef]
46. Guo, J.; Wang, C.; Liu, X.; Chen, Y. Explosion venting of rich hydrogen-air mixtures in a small cylindrical vessel with two symmetrical vents. *Int. J. Hydrogen Energy* **2017**, *42*, 7644–7650. [CrossRef]
47. Li, Y.; Bi, M.; Zhou, Y.; Jiang, H.; Huang, L.; Zhang, K.; Gao, W. Experimental and theoretical evaluation of hydrogen cloud explosion with built-in obstacles. *Int. J. Hydrogen Energy* **2020**, *45*, 28007–28018. [CrossRef]
48. Rui, S.; Wang, C.; Luo, X.; Li, Q.; Zhang, H. Experimental study on the effects of ignition location and vent burst pressure on vented hydrogen-air deflagrations in a cubic vessel. *Fuel* **2020**, *278*, 118342. [CrossRef]
49. Li, Y.; Bi, M.; Zhou, Y.; Zhang, Z.; Zhang, K.; Gao, W. Evaluation of unrestricted hydrogen and hydrogen-methane explosion venting through duct. *Int. J. Hydrogen Energy* **2021**, *46*, 7011–7021. [CrossRef]
50. Zhang, K.; Du, S.; Chen, H.; Wang, J.; Zhang, J.; Guo, Y.; Guo, J. Effect of hydrogen concentration on the vented explosion of hydrogen-air mixtures in a 5 m-long duct. *Process Saf. Environ. Prot.* **2022**, *162*, 978–986. [CrossRef]
51. Wang, Q.; Luo, X.; Wang, C.; Liu, Y.; Zhou, P.; Li, B. Experimental study on external explosion for vented hydrogen deflagration in a rectangular tube with different vent coefficients. *Process Saf. Environ. Prot.* **2022**, *158*, 331–339. [CrossRef]
52. Jiang, Y.; Li, Y.; Zhou, Y.; Jiang, H.; Zhang, K.; Gao, Z.; Gao, W. Investigation on unconfined hydrogen cloud explosion with external turbulence. *Int. J. Hydrogen Energy* **2022**, *47*, 8658–8670. [CrossRef]
53. Chang, X.; Bai, C.; Zhang, B. The effect of gas jets on the explosion dynamics of hydrogen-air mixtures. *Process Saf. Environ. Prot.* **2022**, *162*, 384–394. [CrossRef]
54. Song, X.; Zhang, J.; Liu, Q.; Xu, Q.; Chen, J.; Zhang, D.; Xie, L.; Li, B. Visualization of the external flow field during a vented explosion for hydrogen-air mixtures: Effects of hydrogen concentrations and vent areas. *Fuel* **2022**, *327*, 124965. [CrossRef]
55. Park, B.; Kim, Y. Reenacting the hydrogen tank explosion of a fuel-cell electric vehicle: An experimental study. *Int. J. Hydrogen Energy* **2023**, *48*, 34987–35003. [CrossRef]

56. Kuznetsov, M.; Kobelt, S.; Grune, J.; Jordan, T. Flammability limits and laminar flame speed of hydrogen-air mixtures at sub-atmospheric pressures. *Int. J. Hydrogen Energy* **2012**, *37*, 17580–17588. [CrossRef]
57. Amirante, R.; Distaso, E.; Tamburrano, P.; Reitz, R.D. Laminar flame speed correlations for methane, ethane, propane and their mixtures, and natural gas and gasoline for spark-ignition engine simulations. *Int. J. Engine. Res.* **2017**, *18*, 951–970. [CrossRef]
58. Høiset, S.; Hjertager, B.H.; Solberg, T.; Malo, K. Properties of simulated gas explosions of interest to the structural design process. *Process Saf. Prog.* **1998**, *17*, 278–287. [CrossRef]
59. Louca, L.A.; Boh, J.W. *Research Report 146: Analysis and Design of Profiled Blast Walls*; HSE Books: Norwich, UK, 2004.
60. Cowper, G.; Symonds, P. *Technical Report 28: Strain Hardening and Strain Rate Effects in the Impact Loading of the Cantilever Beams*; Department of Applied Mathematics (Brown University): Providence, RI, USA, 1957.
61. Sohn, J.M.; Kim, S.J.; Seo, J.K.; Kim, B.J.; Paik, J.K. Strength assessment of stiffened blast walls in offshore installations under explosions. *Ships Offshore Struct.* **2016**, *11*, 551–560. [CrossRef]
62. Sohn, J.M.; Kim, S.J.; Kim, B.H.; Paik, J.K. Nonlinear structural consequence analysis of FPSO topside blast walls. *Ocean Eng.* **2013**, *60*, 149–162. [CrossRef]
63. Schleyer, G.K.; Langdon, G.S. *Research Report 124: Pulse Pressure Testing of 1/4 Scale Blast Wall Panels with Connections*; HSE Books: Norwich, UK, 2003.
64. American Petroleum Institute (API). *API RP 2FB: Recommended Practice for the Design of Offshore Facilities Against Fire and Blast Loading*; API: Washington, DC, USA, 2020.
65. Standards Norway. *N-003: Actions and Action Effects*; Standards Norway: Lysaker, Norway, 2007.
66. Kim, S.J.; Sohn, J.M.; Lee, J.C.; Li, C.B.; Seong, D.J.; Paik, J.K. Dynamic Structural Response Characteristics of Stiffened Blast Wall under Explosion Loads. *J. Soc. Nav. Archit. Korea* **2014**, *51*, 380–387. [CrossRef]
67. Hassiotis, S.; Jeong, G.D. Identification of stiffness reductions using natural frequencies. *J. Eng. Mech.* **1995**, *121*, 1106–1113. [CrossRef]
68. Javanmardi, A.; Abadi, R.; Marsono, A.K.; Md Tap, M.; Ibrahim, Z.; Ahmad, A. Correlation of stiffness and natural frequency of precast frame system. *Appl. Mech. Mater.* **2015**, *735*, 141–144. [CrossRef]
69. Fire and Blast Information Group (FABIG). *Technical Note 5: Design Guide for Stainless Steel Blast Walls*; FABIG: Berkshire, UK, 1999.

Disclaimer/Publisher's Note: The statements, opinions and data contained in all publications are solely those of the individual author(s) and contributor(s) and not of MDPI and/or the editor(s). MDPI and/or the editor(s) disclaim responsibility for any injury to people or property resulting from any ideas, methods, instructions or products referred to in the content.